



Identifying the roles of Ru single atoms and nanoclusters for energy-efficient hydrogen production assisted by electrocatalytic hydrazine oxidation

Xiya Guan^a, Qiannan Wu^a, Haibo Li^a, Suyuan Zeng^a, Qingxia Yao^a, Rui Li^a, Hongyan Chen^a, Yao Zheng^{b,*}, Konggang Qu^{a,*}

^a School of Chemistry and Chemical Engineering, Shandong Provincial Key Laboratory/Collaborative Innovation Center of Chemical Energy Storage & Novel Cell Technology, Liaocheng University, Liaocheng 252059, China

^b School of Chemical Engineering and Advanced Materials, The University of Adelaide, Adelaide, SA 5005, Australia

ARTICLE INFO

Keywords:

Ru single atom
Ru nanocluster
Hydrogen evolution
Hydrazine oxidation
Hydrogen energy

ABSTRACT

With a much lower thermodynamic reaction potential, the hydrazine oxidation reaction (HzOR) can be employed as an alternative of water oxidation reaction to integrate with the cathodic hydrogen evolution reaction (HER), accomplishing an energy-efficient H₂ production. The realization of this necessitates the development of the excellent bifunctional electrocatalysts for both HER and HzOR. Herein, a common Ru complex was applied to prepare a Ru/porous N-doped carbon composite (Ru/PNC) simultaneously containing abundant Ru single atoms (SAs) and ultrafine Ru nanoclusters (1.7 nm). Firstly, the new Ru/PNC catalysts containing both metal-metal as well as metal-substrate interactions display superb HER and HzOR activities in alkaline and neutral electrolytes, both greatly surpassing the sole Ru nanoparticles or Ru SAs sample. The controlled experiments and theoretical studies unravel water dissociation and H ad-desorption occurs on Ru SAs and nanoclusters, respectively, involving the proton transfer between them during the HER process, while HzOR is mainly proceeded on Ru SAs sites. Secondly, the alkaline overall hydrazine splitting with Ru/PNC only demands a voltage of 0.19 V to achieve 100 mA cm⁻², demonstrating the huge energy-saving advantage compared with conventional water splitting. Additionally, the hydrogen generation can be readily operated with the hydrazine fuel cell and commercial solar cell with the appreciable H₂ production rate of 32.7 and 27.1 mL cm⁻² h⁻¹, respectively.

1. Introduction

As a high-energy-density and carbon-free energy, hydrogen is an ideal candidate to cope with diminishing fossil fuels and increasing environmental concerns [1]. The overall water splitting (OWS) powered by renewable electricity is deemed as the easiest and cleanest path for sustainable hydrogen generation [2,3], which consists of cathodic hydrogen evolution reaction (HER) and anodic oxygen evolution reaction (OER) [4,5]. Although a multitude of electrocatalysts for HER and OER have been developed, the intrinsic high anodic potential of OER and its sluggish 4e⁻ transfer process are the chief causes of the enormous energy wastage and low water electrolysis efficiency [6,7]. To substitute OER with low-operating-potential reactions is a feasible detour to resolve this issue [8–10]. Impressively, hydrazine oxidation reaction (HzOR, N₂H₄ + 4OH⁻ = N₂ + 4 H₂O + 4e⁻) features very low E⁰ of -0.33

V (vs. RHE) and only produces N₂ [11,12], which can be assembled with HER to construct overall hydrazine splitting (OH₂S) system [13–15], consequently significantly decrease the operating potential of OWS. In this case, the design of superior bifunctional HER and HzOR electrocatalysts is of great importance to advance HzOR-assisted energy-efficient hydrogen production.

To date, transition metals-based bifunctional electrocatalysts have been extensively reported including metal nanoparticles [16], phosphide [17,18], nitride [19,20], sulfide [21,22], selenide [23], although with impressive HzOR activity surpassing commercial Pt/C, most of their HER activity performs inferior to Pt/C [16–21,23]. Additionally, the intrinsic susceptibility handicap of transition metals in corrosive electrolytes may lead to unsatisfactory long-term durability. Comparatively, Ru metal is being an in-demand element due to its Pt-like activity, highly chemical resistance and more affordable price (1/3 of Pt)

* Corresponding authors.

E-mail addresses: yao.zheng01@adelaide.edu.au (Y. Zheng), qkonggang@luc.edu.cn (K. Qu).

<https://doi.org/10.1016/j.apcatb.2022.122145>

Received 31 August 2022; Received in revised form 16 October 2022; Accepted 3 November 2022

Available online 11 November 2022

0926-3373/© 2022 Elsevier B.V. All rights reserved.

[24–27]. In particular, Ru single atoms (SAs) have sparked striking research upsurge and feature strong metal-substrate interaction with specific coordination structures [28–31]. SAs own high unit activity due to the maximized atom utilization rate, but the metallic loading concentration is usually much low and results in the inadequate apparent activity. Additionally, under alkaline or neutral condition, HER consists of the water dissociation and subsequent H^* ad/desorption, and HzOR also involves the stepwise dehydrogenation of N_2H_4 [32,33]. Thus, the catalytic capacity of Ru SAs is constrained as bifunctional electrocatalysts in the reactions with aforesaid multistep processes due to the normally single-function or high-selectivity metal active centers [34].

On the other hand, the variable crystal structures and surfaces endow metal nanoparticles (NPs) with easily tailored electronic property and thus considerable apparent electrocatalytic activity, but their unit activity or turnover frequency (TOF) is often dissatisfied. Therefore, the integration of nanoparticle and SAs into one system can reconcile highly exposed surfaces and large number of active sites together with high unit activity. More particularly, the metal-substrate interaction of SAs and metal-metal interaction of nanoparticles coexisting in the hybrid system would endow electronic modulations with higher freedom degree and thus bring forth multifunctional active sites with divergent electronic properties [35–37]. Additionally, during the preparation, metal SAs are mostly concomitant with metal nanoparticles (NPs) or nanoclusters (NCs) [38,39], this troublesome challenge in the preparation of SAs would be promisingly advantageous instead to design bifunctional electrocatalysts. Therefore, to unclothe the respective roles of concomitant SAs and NPs is indispensable to elaborately fabricate the advanced electrocatalysts and clarify the catalytic mechanisms.

Herein, one common Ru complex, tris(2,2-bipyridine) ruthenium(II) chloride ($Ru(bpy)_3$), was engaged into the preparation of Ru/porous N-doped carbon (Ru/PNC) composite with the commercial silica to introduce pores, which consists of abundant Ru SAs and tiny Ru NCs (1.7 nm), thus synergistically result in the outstanding bifunctionally non-acidic HER and HzOR activity. Remarkably, Ru/PNC separately requires a potential of 1.0 and -20.4 mV to attain 10 mA cm^{-2} for alkaline HER and HzOR, greatly surpassing Pt/C. Moreover, Ru/PNC also exhibits the comparable HER activity with Pt/C and better HzOR activity in neutral electrolyte. Consequently, the two-electrode OH $_2$ S systems show huge energy-saving advantage with the potential difference of above 2.0 V in both electrolytes. The homemade direct N_2H_4/H_2O_2 fuel cell and commercial solar cell can easily drive the alkaline OH $_2$ S system to realize a respective H_2 production rate of 32.7 and 27.1 $\text{mL cm}^{-2}\text{ h}^{-1}$. More deeply experimental and theoretical explorations unclothe the water dissociation occurs on Ru SAs while the subsequent H ad-desorption on Ru NCs accompanied with the proton transfer between them during HER, while Ru SAs responsible for HzOR. The appropriate microenvironments render the Ru active sites with reduced water dissociation energy barrier, optimized ad-desorption free energies of H^* and dehydrogenation intermediates of N_2H_4 .

2. Experimental section

2.1. Preparation of Ru/PNC

In a typical experiment, $Ru(bpy)_3$ and silica with a select ratio were mixed into 80 mL ethanol and stirred for 12 h, which was then dried by rotary evaporation. The collected sample was annealed at 700°C for 1 h at a ramp rate of 5°C min^{-1} under Ar atmosphere. Then, the collected product was soaked in 6 M HF solution for 4 h thrice to completely etched out silica templates, then washed thoroughly and dried, the obtained samples was denoted as Ru/PNC.

2.2. Preparation of Ru SA/NC

6 g dicyandiamide, 1.5 g L-cysteine and 20 mg Ru(III) acetylacetonate were treated by ball-milling with a speed of 400 rpm for 2 h twice at

room temperature [30]. The collected mixture was carbonized at 600°C for 2 h and then 800°C for 1 h with a heating rate of 3°C min^{-1} at Ar atmosphere. The obtained Ru single atom/NC sample was denoted as Ru SA/NC.

2.3. Preparation of Ru/C

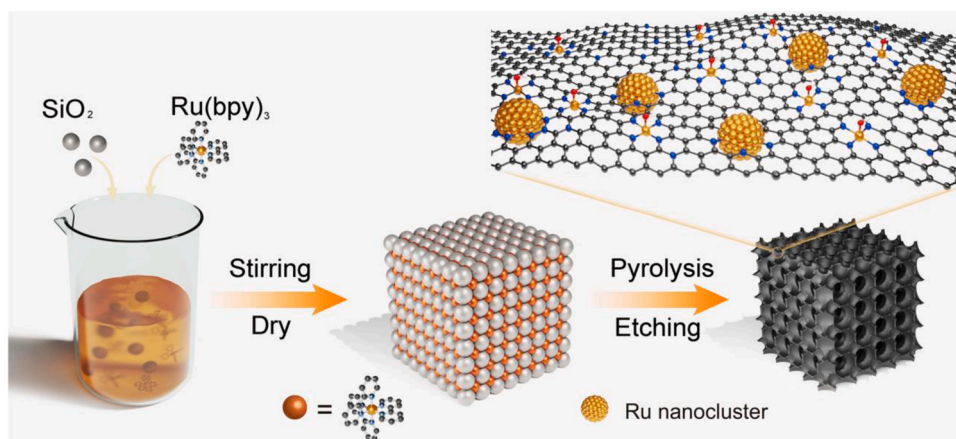
The carbon black (Cabot Vulcan XC-72R, 50 mg) was pretreated with heating in 65 % HNO_3 solution at 60°C for 4 h. A certain amount of $RuCl_3 \cdot xH_2O$ were added into 10 mL ultrapure H_2O , and then ultrasonically mixed with the pretreated carbon black. The 10 mL $NaBH_4$ solution (the molar ration of $NaBH_4$ and Ru is 4:1) was added dropwise to the above suspension under vigorous stirring. The mixture was continuously stirred for another 2 h to achieve the complete reaction. The sample was washed thrice with centrifugation and dried in a vacuum oven at 60°C . The resulted sample was denoted as Ru/C with the Ru loading of 20 wt %.

3. Results and discussion

3.1. Synthesis and characterization

Scheme 1 illustrates the facile synthesis route of Ru/PNC with the simple mixing and pyrolysis. The morphology and microstructure of Ru/PNC was firstly examined by scanning electron microscopy (SEM) and transmission electron microscopy (TEM). As presented in Fig. S1A, SEM image shows the internally porous and discrete bulk morphology. The dense and uniform NCs with the statistically averaging 1.7 nm distribute evenly on honeycomb-like carbon flakes with distinct pores around 10 nm and curly fringes observed by TEM (Fig. 1A and S1B). The high-resolution scanning TEM (STEM) presents an interplanar distance of 0.206 nm coinciding with the (101) lattice plane of Ru (Fig. S1C) [25]. The high-angle annular dark-field STEM (HAADF-STEM) further displays that a large amount of Ru SAs intersperses around well crystalline Ru NCs (Fig. 1B). Additionally, the elemental mapping results undoubtedly demonstrate the coexistence of C, N, O, and Ru components (Fig. S1D). As the controls, the N-doped carbon only loaded with Ru SAs (Ru SA/NC) was synthesized following the reported method as shown in Fig. S2. While for Ru/C, the about 4-nm Ru NPs are well loaded onto the carbon black (Fig. S3). X-ray diffraction patterns present the broad peaks at 44.0° in Ru/PNC and Ru/C because of their small-size nanoparticles of hexagonal Ru crystals, while no obvious peak is found in Ru SA/NC (Fig. S4). N_2 adsorption-desorption isotherms show Ru/PNC exhibits the much higher Brunauer-Emmett-Teller (BET) surface area and pore volume ($792.0\text{ m}^2/\text{g}$ and $1.17\text{ cm}^3/\text{g}$) than those of Ru SA/NC ($120.8\text{ m}^2/\text{g}$ and $0.25\text{ cm}^3/\text{g}$) and Ru/C ($178.6\text{ m}^2/\text{g}$ and $0.43\text{ cm}^3/\text{g}$), together with the average pore size of 8.63 nm with the size peak centered at around 13 nm originating from the employed silica template (Fig. 1C and S5, Table S1). Such high porosity of Ru/PNC would expose maximized active sites and facilitate mass transport and gas evolution, promisingly resulting in the enhanced electrocatalytic performance. Albeit with richly porous structure, Raman spectrum (Fig. S6) suggests a lowest intensity ratio of D band to G band (I_D/I_G) of 0.93, demonstrating the good graphitization for $Ru(bpy)_3$ -derived carbon, possibly because the bulk morphology of Ru/PNC can retain continuous carbon structures and would largely reduce the interfacial resistance and provide the benign conductivity for electrocatalysis. The Ru loading is separately 26.4 wt % and 2.61 wt % for Ru/PNC and Ru SA/NC determined by elemental analysis (Table S2) [24,40].

X-ray photoelectron spectroscopy (XPS) displays the existence of C, N, O and Ru elements (Figs. S7–S9, Table S3). As to Ru/PNC, the N 1s spectra was deconvoluted into four different N species (Fig. S9): pyridinic N (398.0 eV), Ru–N (399.0 eV), pyrrolic N (400.1 eV) and graphitic N (400.8 eV) [30,41]. The high-resolution spectra of Ru 3p contains the peaks with binding energy located at 462.1 and 484.3 eV corresponding to metallic Ru $3p_{3/2}$ and Ru $3p_{1/2}$, whereas the peaks at



Scheme 1. Schematic illustration of the synthesis of Ru/PNC containing Ru SAs and Ru NCs.

464.0 and 486.7 eV come from the $3p_{3/2}$ and $3p_{1/2}$ of Ru-N species. Similarly, the other two peaks located at 466.5 and 488.8 eV coincide with the $3p_{3/2}$ and $3p_{1/2}$ of the Ru-O bond. Noteworthy, the Ru $3p_{3/2}$ peak of Ru/PNC display a positive shift of about 0.4 eV relative to Ru/C, indicating the electronic interplay between Ru and carbon matrix, which endow Ru with a positive charge owing to the higher electronegativity of N in Ru-N bonds [42]. X-ray absorption spectroscopy (XAS) analysis was performed to uncover the coordination environment and chemical states of the Ru species. Fig. 1D presents the Ru K-edge X-ray absorption near-edge structure (XANES) spectra of Ru/PNC, Ru foil and RuO_2 . The absorption edge of Ru/PNC is much close to that of RuO_2 , revealing the highly oxidized state of Ru species [43]. The Fourier transformed (FT) k^2 -weighted extended X-ray absorption fine structure (EXAFS) characterization shown in Fig. 1E suggests that Ru/PNC exhibits two fitted peaks at 1.3 and 1.6 Å, associated with Ru-N and Ru-O bonds with the respective coordination number (CN) of 4.0 and 1.0 (Fig. 1F), along with a Ru-Ru peak at 2.4 Å with the CN of 3.2, much lower than that of bulk Ru (CN=12, Table S4), which is also confirmed by the fitting at K space (Fig. S10). Wavelet transform (WT) was applied to inspect the Ru K-edge EXAFS oscillations (Fig. 1G). The contour plot of Ru/PNC displays the WT intensity maximum at 4.2 Å, in contrast to that of RuO_2 near 5.2 Å⁻¹ associated with Ru-O bond, apparently because of the concurrent Ru-N and Ru-O bonds for Ru/PNC.

3.2. Electrocatalytic HER and HzOR performance

The alkaline HER activity was initially assessed by linear scan voltammetry (LSV) in 1 M KOH [44]. Fig. 2A presents a potential of only -1.0 mV to attain 10 mA cm⁻² for Ru/PNC, obviously better than -28.6 mV of Ru/C, -207.6 mV of Ru SA/NC and -23.5 mV of Pt/C. Additionally, to afford a large current density of 100 mA cm⁻², Ru/PNC just demands a potential of -60.7 mV, the smallest among the test samples. Tafel plots show the consistent behavior (Fig. S11A), thereinto Ru/PNC has the lowest Tafel slope of 20.6 mV dec⁻¹, suggesting the advanced HER kinetics compared to Ru/C (66.6 mV dec⁻¹), Ru SA/NC (180.4 mV dec⁻¹) and Pt/C (65.7 mV dec⁻¹). The electrochemical impedance spectra (EIS) show the smallest charge transfer resistance (R_{ct}) of 0.8 Ω on Ru/PNC, further revealing the superb interfacial charge transfer kinetics (Fig. S11B). The intrinsic specific activity of Ru/PNC was further characterized with the TOF. The electrochemical active surface area (ECSA) and the number of active sites of different catalysts were calculated by Cu underpotential deposition (Fig. 2B and S12) [24, 38]. Fig. 2C presents Ru/PNC giving the TOF values of 15.4 and 36.3 s⁻¹ at the overpotential of 50 and 100 mV, much larger than those of Ru/C (1.21 and 3.10 s⁻¹), Ru SA/NC (0.79 and 1.46 s⁻¹) and Pt/C (1.74 and 3.88 s⁻¹). Furthermore, the constancy of electrocatalyst is also an important parameter for industrialization potential. The LSV curves

after successive 3000 CV cycles exhibits only a very little decline compared with the initial, and the current density also maintains nearly unchangeable within continuous 10 h's test in the chronoamperometry measurement (Fig. 2D). Remarkably, the activity of Ru/PNC outperform reportedly advanced Ru-based materials [45–54], and large-current-density electrocatalysts (Fig. 2E, Table S5) [55–58], those demonstrating the extraordinary HER performance of the as-prepared Ru/PNC catalyst.

The electrochemical evaluation of HzOR activity was then conducted in the 1.0 M KOH containing N_2H_4 . Firstly, the influence of different N_2H_4 concentrations on the activity was examined. As observed in Fig. 3A, there is no evident anodic current in a hydrazine-free solution. On the contrary, the addition of 0.1 M N_2H_4 leads to the drastically increased anodic current, which was then slowly elevated in the concentration range of 0.1–0.5 M. Additionally, the HzOR activity at the small concentrations of N_2H_4 was also investigated. Fig. S13 illustrates the well-established linear dependence ($R^2 = 0.998$) between current density versus concentration of 0 ~ 5 mM, and the detection limit can be defined as low as 46 μM according to the signal-to-noise ratio of 3 [59], enabling Ru/PNC highly promising for the sensitive detection of N_2H_4 analyte. Fig. 3B illustrates the HzOR LSVs in 1.0 M KOH with 0.5 M N_2H_4 . Ru/PNC exhibits great HzOR activity with a current density of 255 mA cm⁻² at 0.2 V, much larger than that of Ru/C (121 mA cm⁻²), Ru SA/NC (8 mA cm⁻²) and Pt/C (38 mA cm⁻²), also outperforming most of previously powdery HzOR catalysts (Table S6). Moreover, a small Tafel slope of 52.8 mV dec⁻¹ is found on Ru/PNC (Fig. S14A), much lower than Ru/C (63.2 mV dec⁻¹), Ru SA/NC (147.7 mV dec⁻¹) and Pt/C (61.9 mV dec⁻¹), implying the most favorable HzOR dynamics. Furthermore, the EIS spectra (Fig. S14B) show that Ru/PNC has a much lowest R_{ct} value of 4.5 Ω compared to that of Ru/C (9.2 Ω), Ru SA/NC (1083.0 Ω) and Pt/C (7.2 Ω), suggesting the most beneficial charge transport during HzOR process. More insights about HzOR can be gained by the Levich equation with LSVs at different rotation speeds in 1 M KOH with 10 mM N_2H_4 [60,61], the electron transfer number (n) can be extracted from the slope of Levich plot with the values between 3.82 and 4.0 when the potential ranging from 0.3 to 0.9 V (Fig. 3C), indicating the overall 4e⁻ transfer process in HzOR. Finally, the long-time durability was then determined as shown in Fig. 3D, it can be seen the nearly unchanged HzOR LSV curves after 3000 cyclic CV sweeps and also no obvious decay during 10 h's chronoamperometry test, demonstrating the robust stability promising for the practical applications.

Similarly, the neutral HER performances were also investigated in 1.0 M PBS (pH=7.0). The recorded LSV curves display the same potential of -13.1 mV on Ru/PNC with Pt/C to achieve 10 mA cm⁻² with a smallest Tafel slope of 30.7 mV dec⁻¹ and a lowest R_{ct} value of 9.3 Ω, suggesting the outstanding neutral HER performance (Fig. S15).

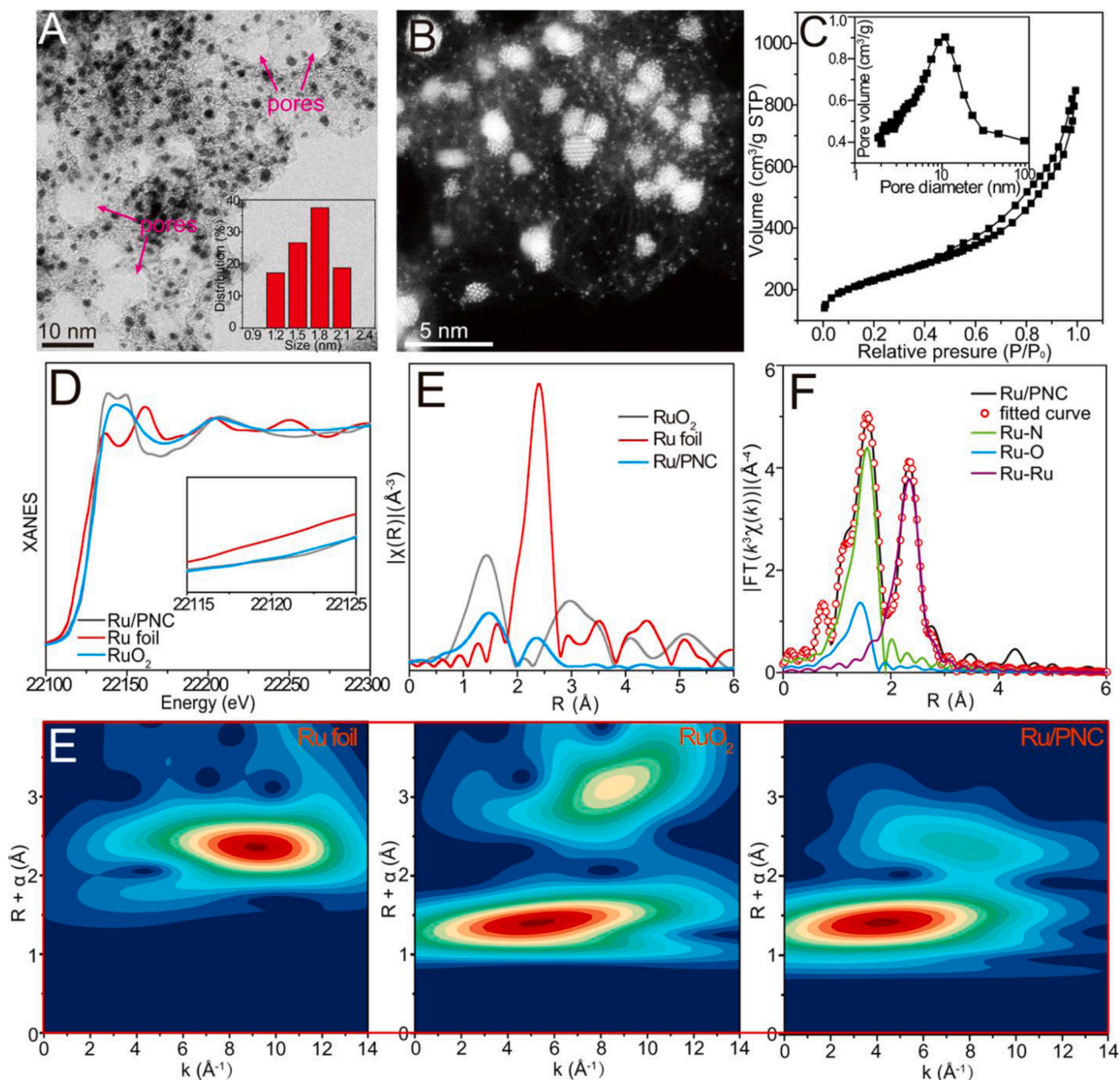


Fig. 1. (A) TEM image with the inset showing the size distribution of Ru NPs. (B) The high-resolution HAADF-STEM images of Ru/PNC. (C) The N₂ adsorption-desorption isotherm and the pore size distribution curve of Ru/PNC. (D) Ru K-edge XANES and (E) Fourier transform (FT) of the Ru K-edge EXAFS spectra of Ru/PNC, Ru foil and RuO₂. (F) The EXAFS fitting results of Ru/PNC at R space. (G) The Ru K-edge WT-EXAFS analyses of Ru/PNC, Ru foil and RuO₂.

Meanwhile, Ru/PNC can retain the nearly unchanged electrocatalytic performance after 3000 CV cycles or during 10 h's chronoamperometric test. Furthermore, the neutral HzOR performance was then examined in 1.0 M PBS with 0.1 M N₂H₄. Fig. 3E reveals Ru/PNC just requires a potential of 177 mV to attain 10 mA cm⁻², far superior to Pt/C (309 mV). Additionally, a small Tafel slope of 53.4 mV dec⁻¹ and a low R_{ct} value of 22.9 Ω confirm a fast kinetics and easy electron transfer for HzOR by Ru/PNC relative to others (Fig. S16). The chronoamperometric and cyclic CV tests also verify the excellent stability of Ru/PNC for neutral HzOR (Fig. 3F).

3.3. Two-electrode OH₂S performance

Encouraged by the superior bifunctional activity and stability toward HER and HzOR, the two-electrode OH₂S system was further investigated using Ru/PNC as the anode and cathode in 1.0 M KOH with 0.5 M N₂H₄

(Fig. 4A). The selected mass loading of Ru/PNC was 0.5 mg cm⁻² on carbon cloth. Fig. 4B shows the OH₂S cell just require a voltage of 0.19 V to achieve 100 mA cm⁻², much smaller than that of Pt/C (0.49 V). Comparatively, an OWS electrolyzer was examined with Ru/PNC as both cathode and anode, which needs a high voltage up to 2.41 V to obtain 100 mA cm⁻², suggesting the superiority of gargantuan energy consumption with OH₂S. Furthermore, the generated H₂ and N₂ were collected using water drainage method with bifunctional Ru/PNC electrode in two-electrode OH₂S cell at 100 mA cm⁻² (Fig. 4C), manifesting near 100 % Faraday efficiency with a perfectly stoichiometric H₂:N₂ ratio of 2:1. Additionally, the hardly any decay of the OH₂S activity was observed for Ru/PNC during a 10 h continuous electrolysis or through 5000 potential cycles (Fig. 4D), showing the two-electrode excellent durability. More importantly, even at a large current density of 100 mA cm⁻² with up to 30 h's operation, no significant degeneration can be detected (Fig. S17), and the post-catalytic samples collected from

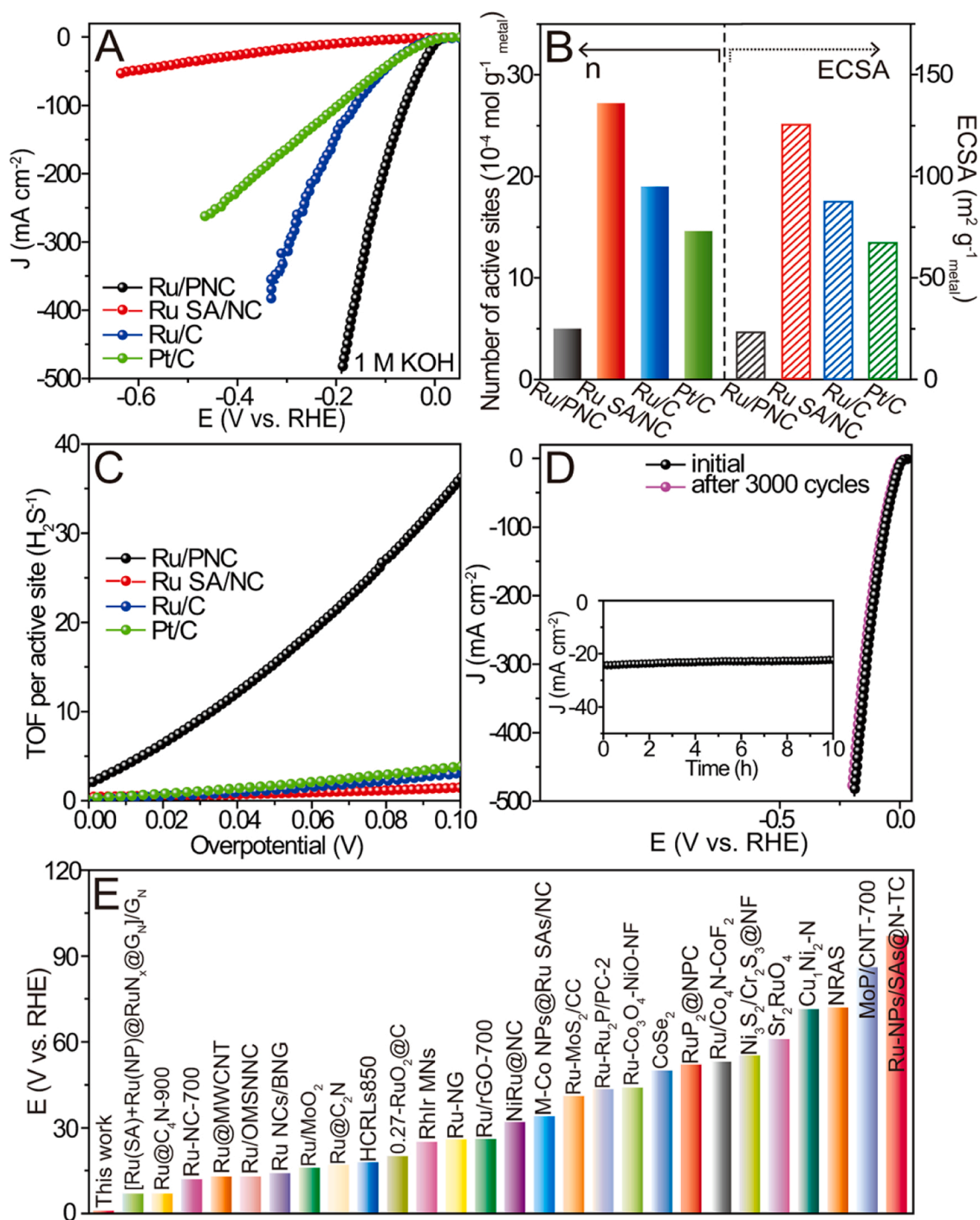


Fig. 2. (A) HER LSV curves, (B) the calculated number of active sites (n) and ECSA using the Cu-UPD method, and (C) the calculated TOF values for alkaline HER on Ru/PNC, Ru SA/NC, Ru/C and Pt/C catalysts, (D) the chronoamperometric test and LSV curves after CV testing of 3000 cycles for HER on Ru/PNC. (E) The comparison of HER activity between Ru/PNC with recently reported electrocatalysts.

the HER and HzOR branches both maintain the initial microstructure (Fig. S18 and S19), suggesting the strong robustness of Ru/PNC [62,63]. Likewise, the two-electrode OH₂S cell in 1.0 M PBS (pH=7.0) with 0.1 M N₂H₄ merely demands 0.22 V to drive 10 mA cm⁻² compared with that of Pt/C (0.41 V), and simultaneously much lower than that of OWS cell (2.17 V) together with the outstanding long-time and cyclic durability (Fig. 4E and F).

3.4. OH₂S performance powered by fuel cell and solar cell

Considering the superior performance of Ru/PNC towards HzOR, the

direct liquid N₂H₄/H₂O₂ fuel cell (DHHPFC) was constructed using Ru/PNC as anode in 4 M KOH/1 M N₂H₄ anolyte and Pt/C as cathode in 0.5 M H₂SO₄/5 M H₂O₂ catholyte, which can be then employed to drive the OH₂S cell as a carbon-free self-powered H₂ production system (Fig. 5A). Expectedly, the Ru/PNC||Pt/C -based battery presents an open-circuit voltage (OCV) of 1.75 V and a power density of 76.50 mW cm⁻² (Fig. 5B and C), much superior to those Pt/C||Pt/C-based battery (1.60 V and 56.30 mW cm⁻²). The integrated DHHPFC-powered OH₂S system (Fig. S20) can be observed with vigorous bubbles in each cell during the operation (movie S1), and yield H₂ with a calculated production rate of 1.46 mmol h⁻¹ (32.7 mL cm⁻² h⁻¹,

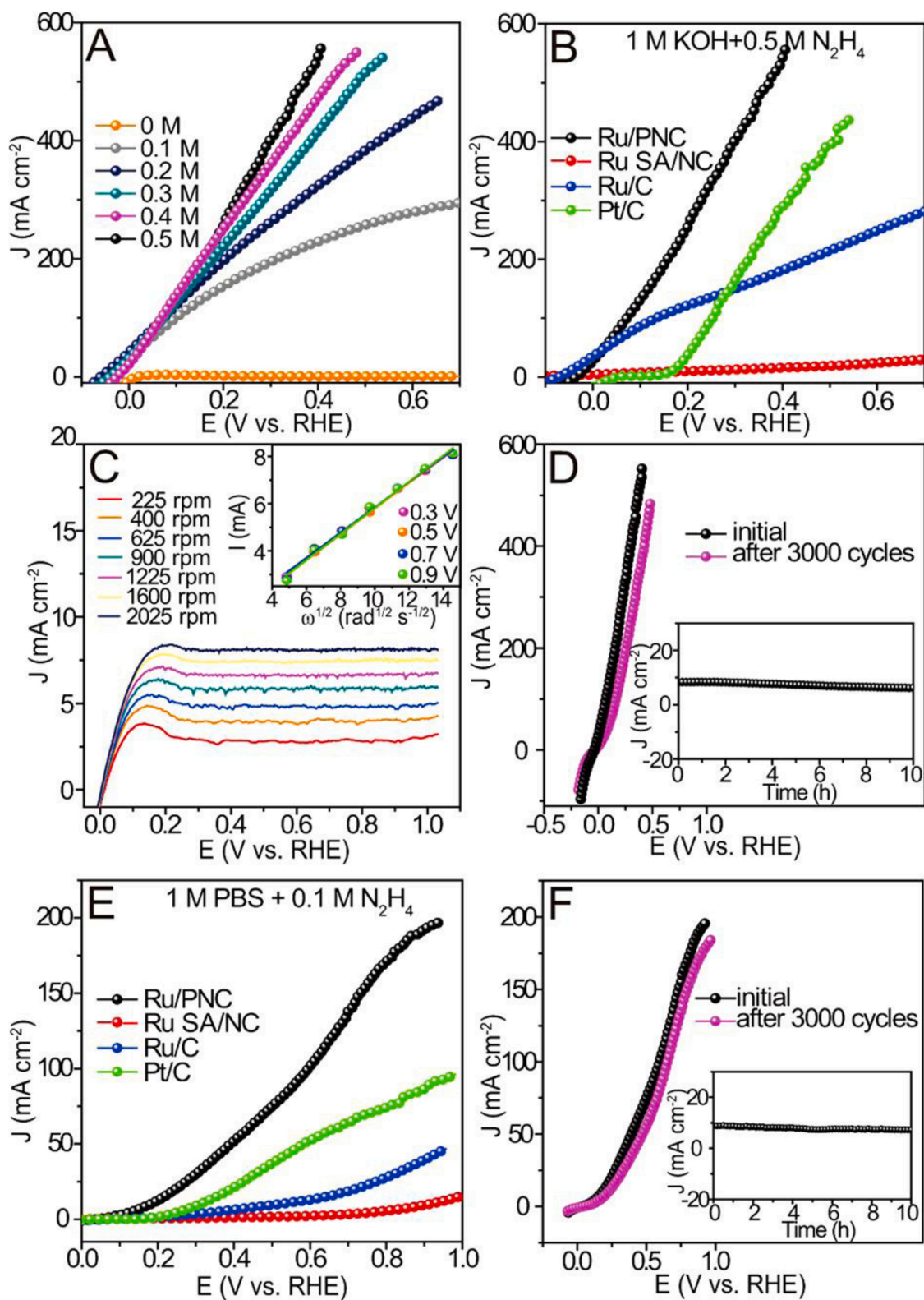


Fig. 3. (A) LSV curves of Ru/PNC in 1.0 M KOH containing different concentrations of hydrazine. (B) HzOR LSV curves in 1 M KOH with 0.5 M N₂H₄, (C) HzOR LSV curves at varied rotation speed in 1 M KOH with 10 mM N₂H₄, and the inset shows the Levich plots at different potentials. (D) the chronoamperometric test and LSV curves after CV testing of 3000 cycles for alkaline HzOR. (E) HzOR LSV curves in 1 M PBS with 0.1 M N₂H₄, (F) the chronoamperometric test and LSV curves after CV testing of 3000 cycles for neutral HzOR.

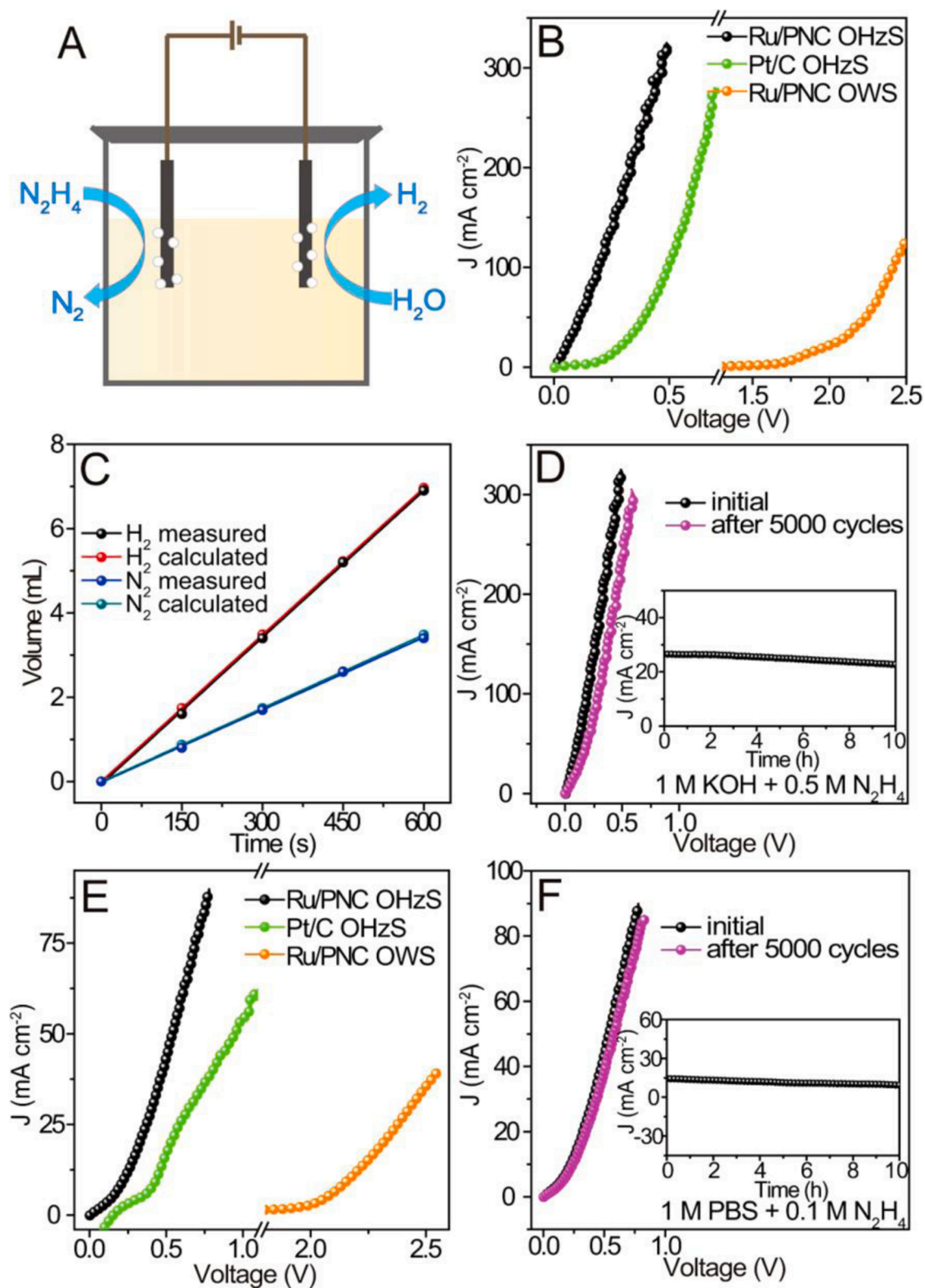


Fig. 4. (A) Schematic illustration of the two-electrode OH₂S electrolyzer. (B) LSV curves of alkaline OH₂S with Ru/PNC and Pt/C as bifunctional electrodes, and LSV curves of OWS with bifunctional Ru/PNC, (C) the amount of H₂ and N₂ theoretically calculated and experimentally measured for Ru/PNC for alkaline OH₂S. (D) the chronoamperometric test and LSV curves after CV testing of 5000 cycles for alkaline OH₂S. (E) LSV curves with Ru/PNC and Pt/C as bifunctional electrodes for neutral OH₂S, and LSV curves of OWS with bifunctional Ru/PNC. (F) the chronoamperometric test and LSV curves after CV testing of 5000 cycles for neutral OH₂S.

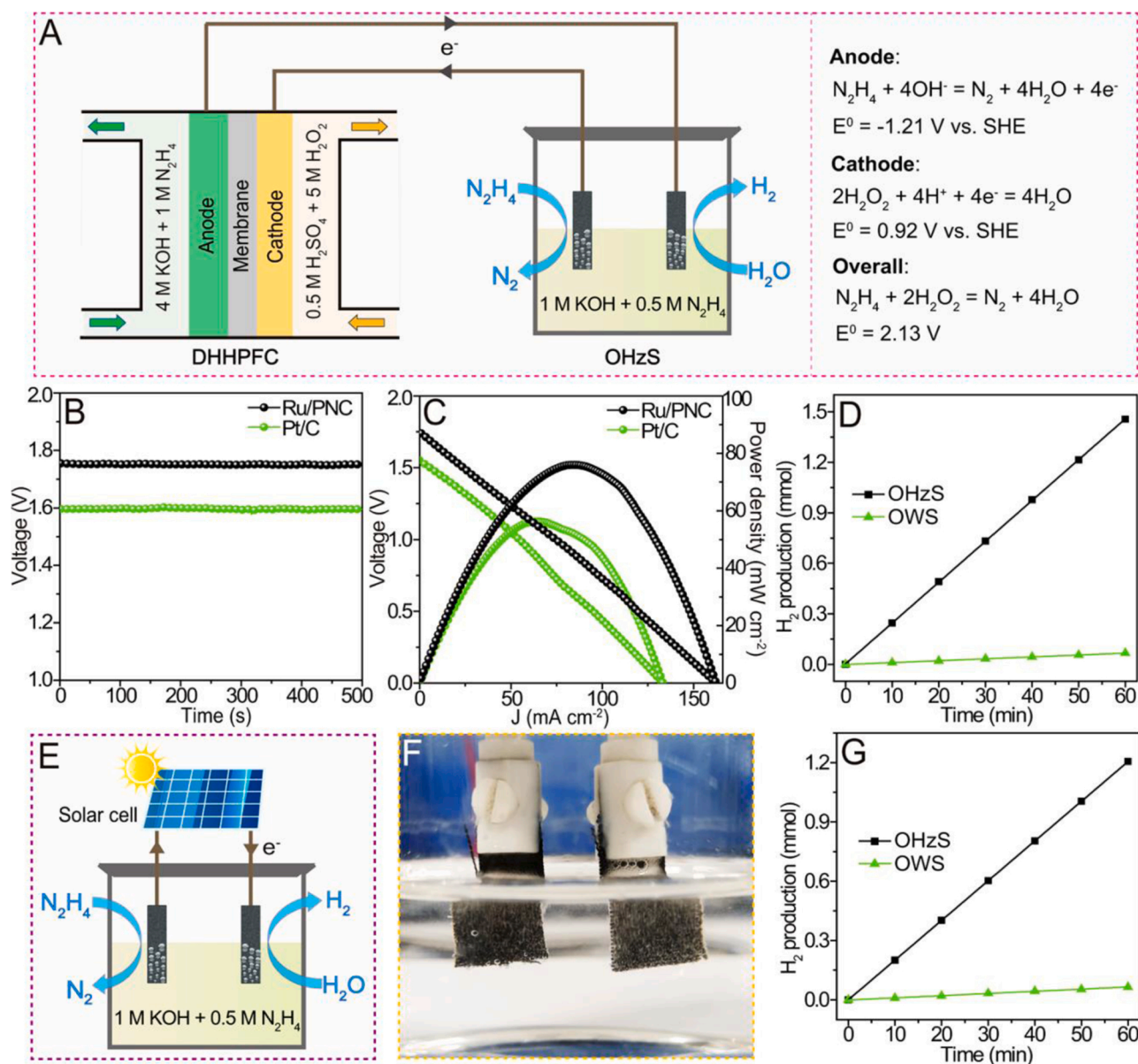


Fig. 5. (A) Schematic illustration and working principle of DHHPPC-powered OHzS system. (B) Open-circuit voltage of the Ru/PNC||Pt/C and Pt/C||Pt/C DHHPPCs. (C) Discharge polarization curve and power density plot of the DHHPPCs. (D) The H_2 production from the DHHPPC-powered OHzS and OWS system. (E) Schematic illustration of the assembled solar cell-powered OHzS system. (F) Digital photograph of the evolution of gas bubbles on bifunctional Ru/PNC electrodes. (G) The H_2 production from the solar cell-powered OHzS and OWS system.

Fig. 5D). Similarly, the solar cell-powered OHzS system was also assembled using commercial polycrystalline silicon solar panel (Fig. 5E and S21). With the irradiation of simulated sunlight, a solar panel with an operating voltage of about 1.5 V can readily drive the OHzS cell with violent bubbles on each electrode (Fig. 5F, movie S2), and the H_2 production can reach up to 1.21 mmol h^{-1} ($27.1 \text{ mL cm}^{-2} \text{ h}^{-1}$, Fig. 5G). In sharp contrast, both DHHPPC- and solar cell-powered OWS systems produce negligible amount of H_2 gas. Therefore, these two kinds of constructed hydrogen production systems demonstrate the versatility of OHzS in energy-efficient practical applications.

Supplementary material related to this article can be found online at [doi:10.1016/j.apcatb.2022.122145](https://doi.org/10.1016/j.apcatb.2022.122145).

3.5. Mechanism investigation

Density functional theory (DFT) computations were then conducted for the insightfully underlying roots for excellent bifunctional behaviors

of Ru/PNC. According to the componential information of Ru/PNC, the structural models were firstly constructed using Ru/N-doped carbon (Ru-NC) representative of nitride Ru NCs, together with three different Ru SA models including RuN_4 , RuN_4OH and RuN_4O to more clearly reveal the electronic property evolution of Ru active sites under subtly different microenvironments (Fig. S22). It's well recognized the non-acidic HER mechanism involves the prior water dissociation of Volmer step and the following coupling of H to H_2 of Tafel step. As presented in Figs. 6A and S23, RuN_4OH possesses a lowest water dissociation energy barrier ($E_{\text{H}_2\text{O}}$) of 0.86 eV, compared with that of Ru-NC (0.92 eV), RuN_4 (1.02 eV) and RuN_4O (2.38 eV), suggesting the most efficient Volmer step on RuN_4OH . For the Tafel step, Ru-NC possessed the most thermoneutral free energy of H adsorption (ΔG_{H}^* , -0.14 eV), compared with that of RuN_4OH (0.18 eV), RuN_4 (-0.75 eV) and RuN_4O (0.87 eV), indicating the most favorable Tafel step in Ru-NC active sites (Fig. 6B). Fig. S24 shows the adsorption energy of different model structures toward H_2O , OH and H, a more favorable adsorption energy of H_2O can be

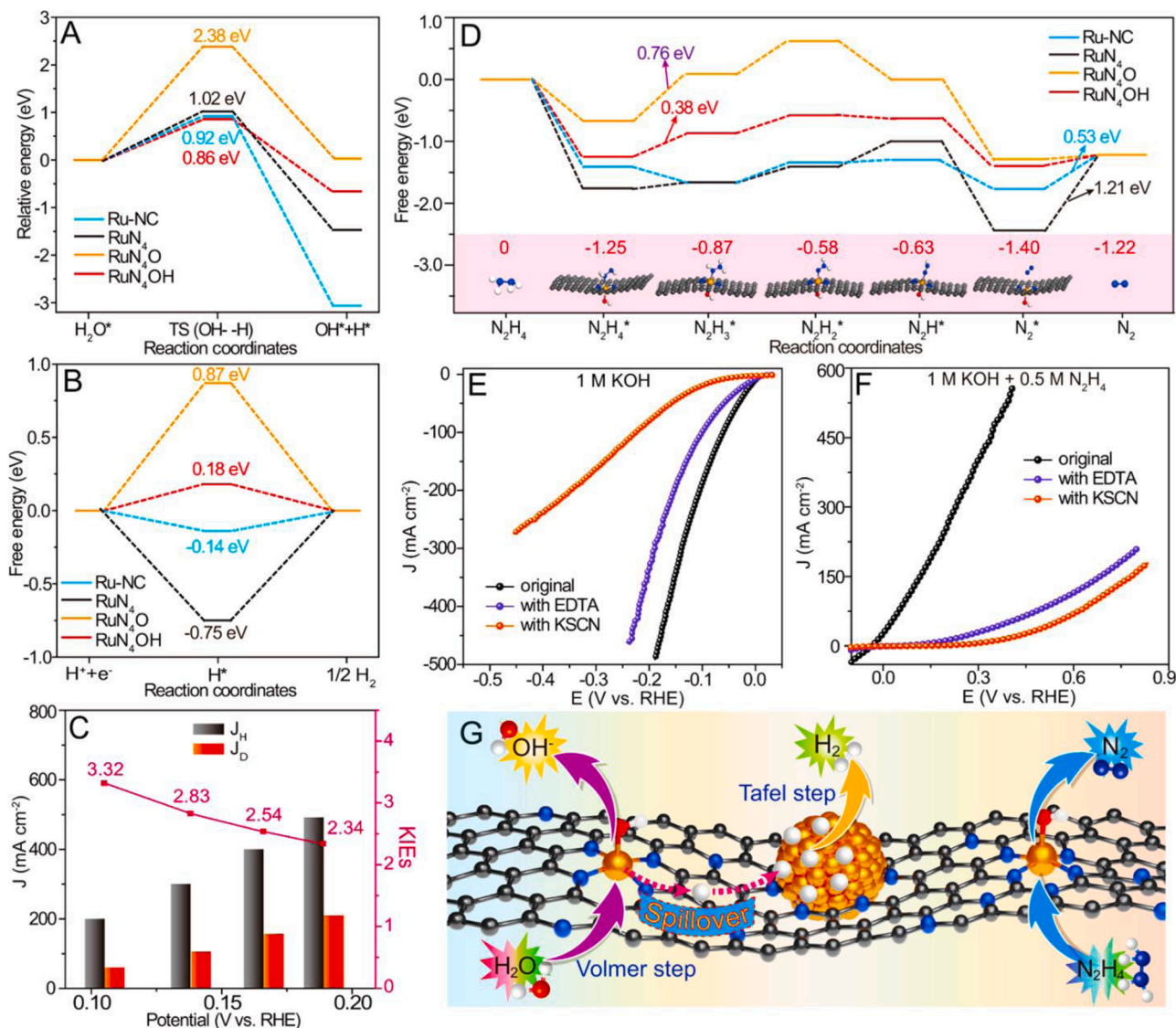


Fig. 6. (A) The calculated energy barriers of water dissociation, (B) the adsorption free energies of H^* and (C) the calculated KIE values from J_H/J_D at different potentials on Ru/PNC. (D) The HzOR pathways and free energy profiles for Ru-NC, RuN₄, RuN₄O and RuN₄OH, and the stepwise hydrazine intermediates on the RuN₄OH surfaces. The brown, gray, blue, red and white sphere stands for Ru, C, N, O and H atom, respectively. LSV curves of Ru/PNC for (E) HER and (F) HzOR with and without 10 mM KSCN and 10 mM EDTA in the alkaline electrolytes. (G) The illustrative mechanisms for non-acidic HER and HzOR.

found on RuN₄OH but with the poorer adsorption towards OH and H, which can not only endow the minimum E_{H_2O} , and also promote the subsequent desorption of produced OH and H and thus keep the active sites always available [64]. The H generated by the decomposition of H₂O on RuN₄OH can be captured by the adjacent nitride Ru NPs due to the moderate adsorption ability to H and then favorably converted into H₂ due to the most thermoneutral ΔG_{H^*} of Ru-NC.

The kinetic isotope effect (KIE) experiments were performed to validate the occurrence of proton transfer during HER. Fig. S25 presents the LSV curves of Ru/PNC in 1.0 M KOH aqueous electrolyte and 1.0 M KOH D₂O electrolyte, and the corresponding KIE values. The KIE values were calculated by the current density ratios from H₂O and D₂O electrolytes (J_H/J_D). When J_H reach 200, 300, 400 and 500 mA cm⁻², the required potential is 0.105, 0.138, 0.166 and 0.189 V, respectively. At above corresponding potentials, the separately measured J_D is 60.4, 106.2, 157.9 and 210.0 (Fig. 6C). Resultantly, the KIE values range from 2.34 to 3.32 (larger than 1.5), evidencing the involvement of proton transfer in the HER steps [65,66]. Additionally, the mixed electrode of WO₃ with Ru/PNC become dark blue after HER, while the sole WO₃ does not (Fig. S26), due to the migrated hydrogen promptly reacting with

WO₃ to produce dark blue H_xWO₃ [66,67]. As aforesaid in Fig. S11 and S15, the extracted value of Tafel slopes is separately 20.6 and 30.7 mV dec⁻¹ for alkaline and neutral HER, which confirms the H desorption into H₂ in Tafel step as the rate-determining step (RDS) on Ru-NC, also suggesting the extremely boosted water dissociation via proton transfer on RuN₄OH with multisite. Contrastingly, Pt/C adopts the Volmer-Heyrovsky route with the water dissociation in Heyrovsky reaction as RDS due to its Tafel slopes close to 40 mV dec⁻¹. Additionally, Ru/PNC also exhibits the superior HER activity in 0.5 M H₂SO₄ on a par with Pt/C (Fig. S27) due to the highly advantageous ΔG_{H^*} , the sole descriptor for acidic HER. Meanwhile, the optimized electrocatalytic descriptors in Ru-NC and RuN₄OH is principally ascribed to the moderate d-band center (ϵ_d) among four models (Fig. S28) regulated by the electron transfer between Ru and carbon substrate or coordinate atoms (Fig. S29), which enable the more delicate balance between the adsorption and desorption for bifunctional catalytic reactions [33].

The HzOR processes on different models were also computed. As shown in Fig. 6D and S30, the decomposition of N₂H₄ relates to consecutive dehydrogenation steps ($N_2H_4 \rightarrow N_2H_4^* \rightarrow N_2H_3^* \rightarrow N_2H_2^* \rightarrow N_2H^* \rightarrow N_2^* \rightarrow N_2$). The exothermic absorption of N₂H₄ and the

endothermic desorption of N_2 were found on all models. However, the dehydrogenation process from $N_2H_4^*$ to $N_2H_3^*$ is the RDS on RuN_4O and RuN_4OH with the respective energy barrier of 0.76 and 0.38 eV. While for $Ru-NC$ and RuN_4 structures, the final desorption of N_2^* to N_2 is the RDS with the uphill energy of 0.53 and 1.21 eV. Resultantly, the RuN_4OH site has the most advantageous kinetics to accomplish the multi-step dehydrogenation process of HzOR. For the further recognition of the contributions from Ru SAs and NCs, KSCN and EDTA poisoning tests were performed because EDTA can only block Ru SAs while SCN^- poisons both [68]. As shown in Fig. 6E and S31A, the HER activity was partially covered by EDTA but the vast majority inhibited by SCN^- . Noteworthy, even in presence of EDTA, the HER activity (10 and 100 $mA\ cm^{-2}$ at 6.0 and 100.2 mV, respectively) still prevails over most of reported HER catalysts (Table S5). This is understandable because the value of E_{H_2O} on $Ru-NC$ is only 0.06 eV higher than that of RuN_4OH , which can also guarantee a relatively smooth decomposition of H_2O even in the case of suppressed RuN_4OH . In stark contrast, the HzOR activity of Ru/PNC can be mostly suppressed by EDTA and thus confirms the dominant contribution of Ru SAs to HzOR activity (Fig. 6F and S31B), coinciding with the DFT calculations. Thus, the non-acidic HER process involves the water dissociation on the Ru SAs and H desorption to form H_2 on Ru NCs together with the H spillover from Ru SAs to Ru NCs, while the HzOR process occurs on Ru SAs (Fig. 6G).

4. Conclusions

In summary, an effortless “mix-and-pyrolysis” approach was proposed to fabricate high-performance Ru/PNC for bifunctional HER and HzOR comprising of rich Ru SAs and tiny Ru NCs together with large surface area and high graphitization. Remarkably, Ru/PNC exhibits much better alkaline and matchable neutral HER activity as well as much better alkaline and neutral HzOR activity compared with Pt/C . Thus, the assembled OH_2S electrolyzers in alkaline and neutral conditions both display a huge energy-saving advantage over OWS with the voltage difference up to 2.0 V at the same current density. The self-powered H_2 production system was exemplified with the OH_2S cell readily driven by the DHPFC and commercial solar cell. The respective roles of Ru SAs and Ru NCs were unveiled with more intensively experimental and theoretical researches, i.e., water dissociates most favorably on Ru SAs while H ad-desorption on Ru NCs along with the concurrent proton transfer between them during HER; Ru SAs own the most optimized ad-desorption free energies of dehydrogenation intermediates of N_2H_4 , all of which can be attributed to the appropriate microenvironments inherited from the employed Ru precursors, endowing the Ru active sites with the optimal electronic properties. This work shed more light on the structure–activity relationship of Ru SAs and NCs and provides the guiding thoughts for the synthesis of advanced electrocatalysts.

CRedit authorship contribution statement

Xiya Guan: Conceptualization, Investigation, Writing – original draft. **Qiannan Wu:** Methodology, Investigation, Data curation. **Haibo Li:** Validation, Funding acquisition. **Suyuan Zeng:** Visualization, Formal analysis. **Qingxia Yao:** Methodology, Data curation. **Rui Li:** Software. **Hongyan Chen:** Resources, Data curation. **Yao Zheng:** Supervision, Project administration, Writing – review & editing. **Konggang Qu:** Supervision, Funding acquisition, Writing – review & editing.

Declaration of Competing Interest

The authors declare no conflict of interest.

Data Availability

Data will be made available on request.

Acknowledgements

This work was financially supported by the Development Project of Youth Innovation Team in Shandong Colleges and Universities (2019KJC031), Natural Science Foundation of Shandong Province (ZR2019MB064 and ZR2021MB122) and Doctoral Program of Liaocheng University (318051608).

Appendix A. Supporting information

Supplementary data associated with this article can be found in the online version at doi:10.1016/j.apcatb.2022.122145.

References

- [1] S. Chu, Y. Cui, N. Liu, The path towards sustainable energy, *Nat. Mater.* 16 (2017) 16–22, <https://doi.org/10.1038/nmat4834>.
- [2] M.F. Lagadee, A. Grimaud, Water electrolyzers with closed and open electrochemical systems, *Nat. Mater.* 19 (2020) 1140–1150, <https://doi.org/10.1038/s41563-020-0788-3>.
- [3] Z.-Y. Yu, Y. Duan, X.-Y. Feng, X. Yu, M.-R. Gao, S.-H. Yu, Clean and affordable hydrogen fuel from alkaline water splitting: past, recent progress, and future prospects, *Adv. Mater.* 33 (2021), 2007100, <https://doi.org/10.1002/adma.202007100>.
- [4] X. Wang, X. Zhou, C. Li, H. Yao, C. Zhang, J. Zhou, R. Xu, L. Chu, H. Wang, M. Gu, H. Jiang, M. Huang, Asymmetric Co-N3P1 trifunctional catalyst with tailored electronic structures enabling boosted activities and corrosion resistance in an uninterrupted seawater splitting system, *Adv. Mater.* 34 (2022), 2204021, <https://doi.org/10.1002/adma.220204021>.
- [5] T. Wang, P. Wang, W. Zang, X. Li, D. Chen, Z. Kou, S. Mu, J. Wang, Nanoframes of Co_3O_4 – Mo_2N heterointerfaces enable high-performance bifunctionality toward both electrocatalytic HER and OER, *Adv. Funct. Mater.* 32 (2022), 2107382, <https://doi.org/10.1002/adfm.202107382>.
- [6] J. Li, Q. Zhou, C. Zhong, S. Li, Z. Shen, J. Pu, J. Liu, Y. Zhou, H. Zhang, H. Ma, Co/Fe) $_2O_4$ cubane-containing nanorings fabricated by phosphorylating cobalt ferrite for highly efficient oxygen evolution reaction, *ACS Catal.* 9 (2019) 3878–3887, <https://doi.org/10.1021/acscatal.9b00293>.
- [7] J. Zhou, Z. Han, X. Wang, H. Gai, Z. Chen, T. Guo, X. Hou, L. Xu, X. Hu, M. Huang, S.V. Levchenko, H. Jiang, Discovery of quantitative electronic structure-OER activity relationship in metal-organic framework electrocatalysts using an integrated theoretical-experimental approach, *Adv. Funct. Mater.* 31 (2021), 2102066, <https://doi.org/10.1002/adfm.202102066>.
- [8] H. Zhao, D. Lu, J. Wang, W. Tu, D. Wu, S.W. Koh, P. Gao, Z.J. Xu, S. Deng, Y. Zhou, B. You, H. Li, Raw biomass electroreforming coupled to green hydrogen generation, *Nat. Commun.* 12 (2021) 2008, <https://doi.org/10.1038/s41467-021-22250-9>.
- [9] Y. Huang, X. Chong, C. Liu, Y. Liang, B. Zhang, Boosting hydrogen production by anodic oxidation of primary amines over a nise nanorod electrode, *Angew. Chem. Int. Ed.* 57 (2018) 13163–13166, <https://doi.org/10.1002/anie.201807717>.
- [10] K. Xiang, D. Wu, X. Deng, M. Li, S. Chen, P. Hao, X. Guo, J.-L. Luo, X.-Z. Fu, Boosting H_2 generation coupled with selective oxidation of methanol into value-added chemical over cobalt Hydroxide@Hydroxysulfide nanosheets electrocatalysts, *Adv. Funct. Mater.* 30 (2020), 1909610, <https://doi.org/10.1002/adfm.201909610>.
- [11] N.K. Janjua, N. Firdous, A.S. Bhatti, Z.S. Khan, Preparation and catalytic evaluation of Ir and Ru catalysts supported in $\gamma-Al_2O_3$ for hydrazine decomposition in a 1N microthruster, *Appl. Catal., A* 479 (2014) 9–16, <https://doi.org/10.1016/j.apcata.2014.04.025>.
- [12] N. Firdous, N.K. Janjua, CoPt $_x$ / $\gamma-Al_2O_3$ bimetallic nanoalloys as promising catalysts for hydrazine electrooxidation, *Heliyon* 5 (2019), e01380, <https://doi.org/10.1016/j.heliyon.2019.e01380>.
- [13] H.-L. Huang, X. Guan, H. Li, R. Li, S. Zeng, S. Tao, Q. Yao, H. Chen, K. Qu, Ir nanoclusters/porous N-doped carbon as a bifunctional electrocatalyst for hydrogen evolution and hydrazine oxidation reactions, *Chem. Commun.* 58 (2022) 2347–2350, <https://doi.org/10.1039/D1CC06972A>.
- [14] G. Feng, L. An, B. Li, Y. Zuo, J. Song, F. Ning, N. Jiang, X. Cheng, Y. Zhang, D. Xia, Atomically ordered non-precious Co_3Ta intermetallic nanoparticles as high-performance catalysts for hydrazine electrooxidation, *Nat. Commun.* 10 (2019) 4514, <https://doi.org/10.1038/s41467-019-12509-7>.
- [15] J. Wang, X. Guan, H. Li, S. Zeng, R. Li, Q. Yao, H. Chen, Y. Zheng, K. Qu, Robust Ru-N metal-support interaction to promote self-powered H_2 production assisted by hydrazine oxidation, *Nano Energy* 100 (2022), 107467, <https://doi.org/10.1016/j.nanoen.2022.107467>.
- [16] Y. Zhu, J. Zhang, Q. Qian, Y. Li, Z. Li, Y. Liu, C. Xiao, G. Zhang, Y. Xie, Dual nanosheets on Ni/C hybrid nanosheet activate superior hydrazine oxidation-assisted high-efficiency H_2 production, *Angew. Chem. Int. Ed.* 61 (2021), e202113082, <https://doi.org/10.1002/anie.202113082>.
- [17] C. Tang, R. Zhang, W. Lu, Z. Wang, D. Liu, S. Hao, G. Du, A.M. Asiri, X. Sun, Energy-saving electrolytic hydrogen generation: Ni_2P nanoarray as a high-performance non-noble-metal electrocatalyst, *Angew. Chem. Int. Ed.* 56 (2017) 842–846, <https://doi.org/10.1002/anie.201608899>.

- [18] T.-J. Wang, G.-R. Xu, H.-Y. Sun, H. Huang, F.-M. Li, P. Chen, Y. Chen, Anodic hydrazine electrooxidation boosted overall water electrolysis by bifunctional porous nickel phosphide nanotubes on nickel foam, *Nanoscale* 12 (2020) 11526–11535, <https://doi.org/10.1039/D0NR02196B>.
- [19] Y. Liu, J. Zhang, Y. Li, Q. Qian, Z. Li, Y. Zhu, G. Zhang, Manipulating dehydrogenation kinetics through dual-doping Co₃N electrode enables highly efficient hydrazine oxidation assisting self-powered H₂ production, *Nat. Commun.* 11 (2020) 1853, <https://doi.org/10.1038/s41467-020-15563-8>.
- [20] Q. Qian, J. Zhang, J. Li, Y. Li, X. Jin, Y. Zhu, Y. Liu, Z. Li, A. El-Harairy, C. Xiao, G. Zhang, Y. Xie, Artificial heterointerfaces achieve delicate reaction kinetics towards hydrogen evolution and hydrazine oxidation catalysis, *Angew. Chem. Int. Ed.* 60 (2021) 5984–5993, <https://doi.org/10.1002/anie.202014362>.
- [21] J. Wang, X. Ma, T. Liu, D. Liu, S. Hao, G. Du, R. Kong, A.M. Asiri, X. Sun, NiS₂ nanosheet array: a high-active bifunctional electrocatalyst for hydrazine oxidation and water reduction toward energy-efficient hydrogen production, *Mater. Today Energy* 3 (2017) 9–14, <https://doi.org/10.1016/j.mtener.2017.02.002>.
- [22] X. Liu, J. He, S. Zhao, Y. Liu, Z. Zhao, J. Luo, G. Hu, X. Sun, Y. Ding, Self-powered H₂ production with bifunctional hydrazine as sole consumable, *Nat. Commun.* 9 (2018) 4365, <https://doi.org/10.1038/s41467-018-06815-9>.
- [23] J.-Y. Zhang, H. Wang, Y. Tian, Y. Yan, Q. Xue, T. He, H. Liu, C. Wang, Y. Chen, B. Y. Xia, Anodic hydrazine oxidation assists energy-efficient hydrogen evolution over a bifunctional cobalt perselenide nanosheet electrode, *Angew. Chem. Int. Ed.* 57 (2018) 7649–7653, <https://doi.org/10.1002/anie.201803543>.
- [24] J. Mahmood, F. Li, S. Jung, M.S. Okyay, I. Ahmad, S. Kim, N. Park, H.Y. Jeong, A. Mah, An efficient and pH-universal ruthenium-based catalyst for the hydrogen evolution reaction, *Nat. Nanotechnol.* 12 (2017) 441–446, <https://doi.org/10.1038/nnano.2016.304>.
- [25] J. Wang, Q. Yu, H. Li, R. Li, S. Zeng, Q. Yao, Z. Guo, H. Chen, K. Qu, Natural DNA-assisted RuP₂ on highly graphitic N,P-codoped carbon for pH-wide hydrogen evolution, *Chem. Commun.* 57 (2021) 7284–7287, <https://doi.org/10.1039/D1CC01951A>.
- [26] Y.-H. Wang, R.-Q. Li, H.-B. Li, H.-L. Huang, Z.-J. Guo, H.-Y. Chen, Y. Zheng, K.-G. Qu, Controlled synthesis of ultrasmall RuP₂ particles on N,P-codoped carbon as superior pH-wide electrocatalyst for hydrogen evolution, *Rare Met.* 40 (2021) 1040–1047, <https://doi.org/10.1007/s12598-020-01665-1>.
- [27] J. Li, C. Zhang, T. Zhang, Z. Shen, Q. Zhou, J. Pu, H. Ma, T. Wang, H. Zhang, H. Fan, Y. Wang, H. Ma, Multiple-interface relay catalysis: enhancing alkaline hydrogen evolution through a combination of Volmer promoter and electrical-behavior regulation, *Chem. Eng. J.* 397 (2020), 125457, <https://doi.org/10.1016/j.cej.2020.125457>.
- [28] J. Li, Y. Li, J. Wang, C. Zhang, H. Ma, C. Zhu, D. Fan, Z. Guo, M. Xu, Y. Wang, H. Ma, Elucidating the critical role of ruthenium single atom sites in water dissociation and dehydrogenation behaviors for robust hydrazine oxidation-boosted alkaline hydrogen evolution, *Adv. Funct. Mater.* 32 (2022), 2109439, <https://doi.org/10.1002/adfm.202109439>.
- [29] J.N. Tiwari, A.M. Harzandi, M. Ha, S. Sultan, C.W. Myung, H.J. Park, D.Y. Kim, P. Thangavel, A.N. Singh, P. Sharma, S.S. Chandrasekaran, F. Salehnia, J.-W. Jang, H.S. Shin, Z. Lee, K.S. Kim, High-performance hydrogen evolution by Ru single atoms and Nitrided-Ru NAnoparticles Implanted on N-Doped graphitic sheet, *Adv. Energy Mater.* 9 (2019), 1900931, <https://doi.org/10.1002/aenm.201900931>.
- [30] H. Qi, J. Yang, F. Liu, L. Zhang, J. Yang, X. Liu, L. Li, Y. Su, Y. Liu, R. Hao, A. Wang, T. Zhang, Highly selective and robust single-atom catalyst Ru1/NC for reductive amination of aldehydes/ketones, *Nat. Commun.* 12 (2021) 3295, <https://doi.org/10.1038/s41467-021-23429-w>.
- [31] J. Li, C. Zhang, H. Ma, T. Wang, Z. Guo, Y. Yang, Y. Wang, H. Ma, Modulating interfacial charge distribution of single atoms confined in molybdenum phosphosulfide heterostructures for high efficiency hydrogen evolution, *Chem. Eng. J.* 414 (2021), 128834, <https://doi.org/10.1016/j.cej.2021.128834>.
- [32] S. Ye, F. Luo, T. Xu, P. Zhang, H. Shi, S. Qin, J. Wu, C. He, X. Ouyang, Q. Zhang, J. Liu, X. Sun, Boosting the alkaline hydrogen evolution of Ru nanoclusters anchored on B/N-doped graphene by accelerating water dissociation, *Nano Energy* 68 (2020), 104301, <https://doi.org/10.1016/j.nanoen.2019.104301>.
- [33] Q. Qian, J. Zhang, J. Li, Y. Li, X. Jin, Y. Zhu, Y. Liu, Z. Li, A. El-Harairy, C. Xiao, Artificial heterointerfaces achieve delicate reaction kinetics towards hydrogen evolution and hydrazine oxidation catalysis, *Angew. Chem. Int. Ed.* 60 (2021) 5984–5993, <https://doi.org/10.1002/anie.202014362>.
- [34] J. Yang, W. Li, D. Wang, Y. Li, Electronic metal-support interaction of single-atom catalysts and applications in electrocatalysis, *Adv. Mater.* 32 (2020), 2003300, <https://doi.org/10.1002/adma.202003300>.
- [35] J. Shan, C. Ye, Y. Jiang, M. Jaroniec, Y. Zheng, S.-Z. Qiao, Metal-metal interactions in correlated single-atom catalysts, *Sci. Adv.* 8 (2022) eabo0762, <https://doi.org/10.1126/sciadv.abo0762>.
- [36] J. Li, C. Zhang, C. Zhang, H. Ma, Z. Guo, C. Zhong, M. Xu, X. Wang, Y. Wang, H. Ma, J. Qiu, Green electrosynthesis of 5,5'-Azotetrazolate energetic materials plus energy-efficient hydrogen production using ruthenium single-atom catalysts, *Adv. Mater.* 34 (2022), 2203900, <https://doi.org/10.1002/adma.202203900>.
- [37] J. Li, C. Zhang, C. Zhang, H. Ma, Y. Yang, Z. Guo, Y. Wang, H. Ma, Electronic configuration of single ruthenium atom immobilized in urchin-like tungsten trioxide towards hydrazine oxidation-assisted hydrogen evolution under wide pH media, *Chem. Eng. J.* 430 (2022), 132953, <https://doi.org/10.1016/j.cej.2021.132953>.
- [38] C. Hu, E. Song, M. Wang, W. Chen, F. Huang, Z. Feng, J. Liu, J. Wang, Partial-single-atom, partial-nanoparticle composites enhance water dissociation for hydrogen evolution, *Adv. Sci.* 8 (2021), 2001881, <https://doi.org/10.1002/advs.202001881>.
- [39] H. Yao, X. Wang, K. Li, C. Li, C. Zhang, J. Zhou, Z. Cao, H. Wang, M. Gu, M. Huang, H. Jiang, Strong electronic coupling between ruthenium single atoms and ultrafine nanoclusters enables economical and effective hydrogen production, *Appl. Catal. B Environ.* 312 (2022), 121378, <https://doi.org/10.1016/j.apcatb.2022.121378>.
- [40] D.H. Kweon, M.S. Okyay, S.-J. Kim, J.-P. Jeon, H.-J. Noh, N. Park, J. Mahmood, J.-B. Baek, Ruthenium anchored on carbon nanotube electrocatalyst for hydrogen production with enhanced Faradaic efficiency, *Nat. Commun.* 11 (2020) 1278, <https://doi.org/10.1038/s41467-020-15069-3>.
- [41] Q. Yu, J. Wang, H. Li, R. Li, S. Zeng, R. Li, Q. Yao, H. Chen, K. Qu, Y. Zheng, Natural DNA-derived highly-graphitic N, P, S-tridoped carbon nanosheets for multiple electrocatalytic applications, *Chem. Eng. J.* 429 (2022), 132102, <https://doi.org/10.1016/j.cej.2021.132102>.
- [42] Q. Wu, M. Luo, J. Han, W. Peng, Y. Zhao, D. Chen, M. Peng, J. Liu, F.M.F. de Groot, Y. Tan, Identifying electrocatalytic sites of the nanoporous copper–ruthenium alloy for hydrogen evolution reaction in alkaline electrolyte, *ACS Energy Lett.* 5 (2020) 192–199, <https://doi.org/10.1021/acsenergylett.9b02374>.
- [43] B. Lu, L. Guo, F. Wu, Y. Peng, J.E. Lu, T.J. Smart, N. Wang, Y.Z. Finfrock, D. Morris, P. Zhang, N. Li, P. Gao, Y. Ping, S. Chen, Ruthenium atomically dispersed in carbon outperforms platinum toward hydrogen evolution in alkaline media, *Nat. Commun.* 10 (2019) 631, <https://doi.org/10.1038/s41467-019-08419-3>.
- [44] Q. Yu, H. Li, R. Li, S. Zeng, R. Li, Q. Yao, H. Chen, K. Qu, Y. Zheng, Natural DNA-assisted ultrafine FeP embedded in N, P-codoped carbons for efficient oxygen reduction, hydrogen evolution and rechargeable zinc-air battery, *Carbon* 186 (2022) 171–179, <https://doi.org/10.1016/j.carbon.2021.09.064>.
- [45] H. Li, K. Liu, J. Fu, K. Chen, K. Yang, Y. Lin, B. Yang, Q. Wang, H. Pan, Z. Cai, H. Li, M. Cao, J. Hu, Y.-R. Lu, T.-S. Chan, E. Cortés, A. Fratallocchi, M. Liu, Paired Ru-O-Mo ensemble for efficient and stable alkaline hydrogen evolution reaction, *Nano Energy* 82 (2021), 105767, <https://doi.org/10.1016/j.nanoen.2021.105767>.
- [46] Y. Li, Y. Luo, Z. Zhang, Q. Yu, C. Li, Q. Zhang, Z. Zheng, H. Liu, B. Liu, S. Dou, Implanting Ru nanoclusters into N-doped graphene for efficient alkaline hydrogen evolution, *Carbon* 183 (2021) 362–367, <https://doi.org/10.1016/j.carbon.2021.07.039>.
- [47] Z. Liu, Z. Li, J. Li, J. Xiong, S. Zhou, J. Liang, W. Cai, C. Wang, Z. Yang, H. Cheng, Engineering of Ru/Ru₂P interfaces superior to Pt active sites for catalysis of the alkaline hydrogen evolution reaction, *J. Mater. Chem. A* 7 (2019) 5621–5625, <https://doi.org/10.1039/C8TA11635K>.
- [48] J. Mahmood, F. Li, S.-M. Jung, M.S. Okyay, I. Ahmad, S.-J. Kim, N. Park, H. Y. Jeong, J.-B. Baek, An efficient and pH-universal ruthenium-based catalyst for the hydrogen evolution reaction, *Nat. Nanotechnol.* 12 (2017) 441–446, <https://doi.org/10.1038/nnano.2016.304>.
- [49] A. Maiti, S.K. Srivastava, N. Ru codoped pellet drum bundle-Like Sb₂S₃: an efficient hydrogen evolution reaction and hydrogen oxidation reaction electrocatalyst in alkaline medium, *ACS Appl. Mater. Inter.* 12 (2020) 7057–7070, <https://doi.org/10.1021/acsaami.9b17368>.
- [50] Z. Pu, I.S. Amiin, Z. Kou, W. Li, S. Mu, RuP₂-Based catalysts with platinum-like activity and higher durability for the hydrogen evolution reaction at all pH values, *Angew. Chem. Int. Ed.* 56 (2017) 11559–11564, <https://doi.org/10.1002/anie.201704911>.
- [51] J. Wang, W. Fang, Y. Hu, Y. Zhang, J. Dang, Y. Wu, B. Chen, H. Zhao, Z. Li, Single atom Ru doping 2H-MoS₂ as highly efficient hydrogen evolution reaction electrocatalyst in a wide pH range, *Appl. Catal. B Environ.* 298 (2021), 120490, <https://doi.org/10.1016/j.apcatb.2021.120490>.
- [52] B. Yan, D. Liu, X. Feng, M. Shao, Y. Zhang, Ru species supported on MOF-Derived N-Doped TiO₂/C hybrids as efficient electrocatalytic/photocatalytic hydrogen evolution reaction catalysts, *Adv. Funct. Mater.* 30 (2020), 2003007, <https://doi.org/10.1002/adfm.202003007>.
- [53] S. Zhou, H. Jang, Q. Qin, Z. Li, M. Gyu Kim, X. Ji, X. Liu, J. Cho, Ru atom-modified Co₄N-CoF₂ heterojunction catalyst for high-performance alkaline hydrogen evolution, *Chem. Eng. J.* 414 (2021), 128865, <https://doi.org/10.1016/j.cej.2021.128865>.
- [54] M. You, X. Du, X. Hou, Z. Wang, Y. Zhou, H. Ji, L. Zhang, Z. Zhang, S. Yi, D. Chen, In-situ growth of ruthenium-based nanostructure on carbon cloth for superior electrocatalytic activity towards HER and OER, *Appl. Catal. B Environ.* 317 (2022), 121729, <https://doi.org/10.1016/j.apcatb.2022.121729>.
- [55] T. Kou, S. Wang, R. Shi, T. Zhang, S. Chiovoloni, J.Q. Lu, W. Chen, M.A. Worsley, B. C. Wood, S.E. Baker, E.B. Duoss, R. Wu, C. Zhu, Y. Li, Periodic porous 3D electrodes mitigate gas bubble traffic during alkaline water electrolysis at high current densities, *Adv. Energy Mater.* 10 (2020), 2002955, <https://doi.org/10.1002/aenm.202002955>.
- [56] Y. Yao, Y. Zhu, C. Pan, C. Wang, S. Hu, W. Xiao, X. Chi, Y. Fang, J. Yang, H. Deng, S. Xiao, J. Li, Z. Luo, Y. Guo, Interfacial sp C–O–Mo hybridization originated high-current density hydrogen evolution, *J. Am. Chem. Soc.* 143 (2021) 8720–8730, <https://doi.org/10.1021/jacs.1c02831>.
- [57] D. Wu, D. Chen, J. Zhu, S. Mu, Ultralloy Ru incorporated amorphous cobalt-based oxides for high-current-density overall water splitting in alkaline and seawater media, *Small* 17 (2021), 2102777, <https://doi.org/10.1002/sml.202102777>.
- [58] H.Q. Fu, M. Zhou, P.F. Liu, P. Liu, H. Yin, K.Z. Sun, H.G. Yang, M. Al-Mamun, P. Hu, H.-F. Wang, H. Zhao, Hydrogen spillover-bridged volmer/tafel processes enabling ampere-level current density alkaline hydrogen evolution reaction under low overpotential, *J. Am. Chem. Soc.* 144 (2022) 6028–6039, <https://doi.org/10.1021/jacs.2c01094>.
- [59] A. Mujtaba, N.K. Janjua, T. Yasin, S. Sabahat, Assessing the electrochemical performance of hierarchical nanostructured CuO/TiO₂ as an efficient bifunctional electrocatalyst, *J. Iran. Chem. Soc.* 17 (2020) 649–662, <https://doi.org/10.1007/s13738-019-01797-x>.

- [60] D.A. Finkelstein, R. Imbeault, S. Garbarino, L. Roué, D. Guay, Trends in catalysis and catalyst cost effectiveness for N_2H_4 fuel cells and sensors: a Rotating Disk Electrode (RDE) study, *J. Phys. Chem. C*. 120 (2016) 4717–4738, <https://doi.org/10.1021/acs.jpcc.5b10156>.
- [61] K. Ojha, E.M. Farber, T.Y. Burshtein, D. Eisenberg, A multi-doped electrocatalyst for efficient hydrazine oxidation, *Angew. Chem. Int. Ed.* 57 (2018) 17168–17172, <https://doi.org/10.1002/anie.201810960>.
- [62] S. Wen, J. Huang, T. Li, W. Chen, G. Chen, Q. Zhang, X. Zhang, Q. Qian, K. Ostrikov, Multiphase nanosheet-nanowire cerium oxide and nickel-cobalt phosphide for highly-efficient electrocatalytic overall water splitting, *Appl. Catal. B Environ.* 316 (2022), 121678, <https://doi.org/10.1016/j.apcatb.2022.121678>.
- [63] X. Guo, X. Wan, Q. Liu, Y. Li, W. Li, J. Shui, Phosphated IrMo bimetallic cluster for efficient hydrogen evolution reaction, *eScience* 2 (2022) 304–310, <https://doi.org/10.1016/j.esci.2022.04.002>.
- [64] J. Mao, C.-T. He, J. Pei, W. Chen, D. He, Y. He, Z. Zhuang, C. Chen, Q. Peng, D. Wang, Y. Li, Accelerating water dissociation kinetics by isolating cobalt atoms into ruthenium lattice, *Nat. Commun.* 9 (2018) 4958, <https://doi.org/10.1038/s41467-018-07288-6>.
- [65] W. Li, F. Li, H. Yang, X. Wu, P. Zhang, Y. Shan, L. Sun, A bio-inspired coordination polymer as outstanding water oxidation catalyst via second coordination sphere engineering, *Nat. Commun.* 10 (2019) 5074, <https://doi.org/10.1038/s41467-019-13052-1>.
- [66] J. Dai, Y. Zhu, Y. Chen, X. Wen, M. Long, X. Wu, Z. Hu, D. Guan, X. Wang, C. Zhou, Q. Lin, Y. Sun, S.-C. Weng, H. Wang, W. Zhou, Z. Shao, Hydrogen spillover in complex oxide multifunctional sites improves acidic hydrogen evolution electrocatalysis, *Nat. Commun.* 13 (2022) 1189, <https://doi.org/10.1038/s41467-022-28843-2>.
- [67] Q. Shen, H. Jin, P. Li, X. Yu, L. Zheng, W. Song, C. Cao, Breaking the activity limitation of iridium single-atom catalyst in hydrogenation of quinoline with synergistic nanoparticles catalysis, *Nano Res.* 15 (2022) 5024–5031, <https://doi.org/10.1007/s12274-022-4235-4>.
- [68] X. Wang, Z. Chen, Z. Han, H. Gai, J. Zhou, Y. Wang, P. Cui, J. Ge, W. Xing, X. Zheng, M. Huang, H. Jiang, Manipulation of new married edge-adjacent Fe_2N_5 catalysts and identification of active species for oxygen reduction in wide pH range, *Adv. Funct. Mater.* 32 (2022), 2111835, <https://doi.org/10.1002/adfm.202111835>.